Segmentation of ultrasound images of the carotid using RANSAC and cubic splines

Rui Rocha [a,b,*], Aurélio Campilho [a,c], Jorge Silva [a,c], Elsa Azevedo [d,e], Rosa Santos [e]

[a] INEB - Instituto de Engenharia Biomédica, Porto, Portugal
[b] ISEP - Instituto Superior de Engenharia do Porto, Porto, Portugal
[c] FEUP - Universidade do Porto, Faculdade de Engenharia, Porto, Portugal
[d] FMUP - Universidade do Porto, Faculdade de Medicina, Porto, Portugal
[e] HSJ - Hospital de São João, Dep. de Neurologia, Porto, Portugal

ARTICLE INFO

ABSTRACT

A new algorithm is proposed for the semi-automatic segmentation of the near-end and the far-end adventitia boundary of the common carotid artery in ultrasound images. It uses the random sample consensus method to estimate the most significant cubic splines fitting the edge map of a longitudinal section. The consensus of the geometric model (a spline) is evaluated through a new gain function, which integrates the responses to different discriminating features of the carotid boundary: the proximity of the geometric model to any edge or to valley shaped edges; the consistency between the orientation of the normal to the geometric model and the intensity gradient; and the distance to a rough estimate of the lumen boundary.

A set of 50 longitudinal B-mode images of the common carotid and their manual segmentations performed by two medical experts were used to assess the performance of the method. The image set was taken from 25 different subjects, most of them having plaques of different classes (class II to class IV), sizes and shapes.

The quantitative evaluation showed promising results, having detection errors similar to the ones observed in manual segmentations for 95% of the far-end boundaries and 73% of the near-end boundaries.

© 2011 Elsevier Ireland Ltd. All rights reserved.

1. Introduction

Non-invasive ultrasound imaging of human arteries is a widely used form of medical diagnosis of arterial diseases, like atherosclerosis, a disease of blood vessels caused by the formation of plaques inside the arteries. Atherosclerosis is quantitatively evaluated by the intima-media thickness (IMT), which measures the distance between the inner boundary of the adventitia and the lumen, the region of the vessel where the blood flows. The IMT of extracranial carotid arteries, which can be measured using B-mode imaging, provides an index of individual atherosclerosis and is used for cardiovascular risk assessment in clinical practice [1]. The diagnosis of atherosclerosis is one of the most important medical examinations for the prevention of cardiovascular events, like myocardial infarction and stroke [2,3]. However, it requires the detection of both the adventitia and the lumen boundaries. This is not the case with other forms of diagnosis of arterial diseases, like the assessment of the carotid diameter waveform [4], where only the detection of the adventitia boundaries are required. Therefore, there is also an obvious interest in automatic

algorithms for the segmentation of the adventitia boundaries on their own, in B-mode images of the carotid.

Since the carotid is a superficial artery, it is quite suited for medical ultrasound imaging. B-mode images are user dependent and have very poor quality due to some degrading factors such as [5,6]: speckle, echo shadows, attenuation, low contrast and movement artifacts. However, this technique has lower cost and smaller risk to the patient, when compared to alternative methods like X-ray angiography, intravascular ultrasound, magnetic resonance imaging or computer tomography [5,7].

Medical ultrasound images are a huge challenge to automatic segmentation since they are extremely noisy and large parts of the edges may be missing, producing gaps in organ boundaries. The segmentation of the carotid artery has three additional difficulties. First, the carotid may appear with severe and unpredictable bending along its major axis. Second, scans may correspond to different regions of the carotid, showing different anatomical structures. Third, the artery lumen may appear with occlusions caused by plaques. Due to the variability of the carotid shape and the possible existence of extensive occlusions, most of the known model-based segmentation techniques [8–11] are inadequate. This was one of the reasons that motivated the search for a new segmentation algorithm.

In B-mode images, the carotid adventitia is characterized by two almost parallel echogenic lines separated by a hypoechogenic space, an intensity valley shaped edge known as the 'double line' pattern [12].

The bifurcation and the internal carotid artery (ICA) are more prone to atherosclerosis, due to stronger hemodynamic stresses in the bifurcation and branching zones. Unfortunately, it is difficult to visualize the 'double line' pattern at these locations. For these reasons, IMT measurements in B-mode images are often made over the common carotid artery (CCA), both in clinical practice and in computerized methods [12]. In the first published attempts to detect the carotid boundaries in ultrasound images [13–15], an initial manual segmentation of the boundary was needed. The location of the boundary was then refined, according to the local value of a single image feature, like the echo intensity or the intensity gradient. These approaches suffered from two important weaknesses: the large manual intervention and the use of a single image feature, which is not enough to correctly detect the carotid boundaries in B-mode images.

More powerful approaches were proposed in [16,17]. A common characteristic of these approaches is the use of dynamic programming (DP) for the minimization of a global cost function integrating multiple image features. These models produce more robust segmentations, with less human intervention, specially in the case of [16]. In a later study [18], the DP algorithm proposed in [16] showed better performance when compared with alternative approaches using the maximum gradient [15] and a matched filter [19].

An improvement of [16] was proposed in [20] by embedding DP in a multiscale scheme, to get a first rough estimate of the carotid wall boundaries, and integrating an external force in the cost function. This model was tested against a large data set with promising results and has the advantage of being relatively fast. But it has several important drawbacks: its performance is significantly affected by the presence of plaque and other boundaries; frequently, human correction is needed when the quality of the images is poor; computing the optimal weights of the cost function requires an exhaustive search and different weights have to be computed for each boundary; DP implementations are not suited for embedding global smoothness constraints.

Another family of algorithms [21–23] tried to apply parametric snakes [24] to the detection of the carotid boundaries. However, these techniques do not seem to be the best choice for the segmentation of the carotid wall. First, they usually require a manual initialization in a close vicinity of the carotid boundaries. Second, the propagation force is frequently based on intensity gradients, making the snake very vulnerable to false edges. Third, these snakes usually leak at wall gaps where the gradient is too weak.

In [21], the leaking problem was avoided by discarding all images with large boundary gaps. The authors also excluded the images where the lumen boundary or the carotid wall boundary could not be defined visually. The snake had to be initialized manually and the intensity gradient was the only image feature considered in the energy of the snake.

A more sophisticated external force was used in [22,23], but it is also based on the intensity gradient, which means the snake is still sensitive to local noise and to boundary gaps. Only the far-end boundary is detected and the user just has to specify the starting and the end points of the snake, significantly reducing human intervention. From an initial contour, the snake finds the final location of the lumen boundary. To detect the wall boundary, the snake is slightly displaced downwards and a new search is done for the global minimum of the snake's energy. Some results were presented but the work lacks a validation with statistical meaning. Despite the previous attempts, there is still no standard procedure for the automatic detection of the carotid boundaries in B-mode images. Therefore, the usual approach is manual segmentation performed by a specialist (see, for instance, [25,26]), which is time consuming and prone to subjectivity.

In this paper, a new method is introduced for the semi-automatic segmentation of the near-end (NE) and the far-end (FE) adventitia boundary in longitudinal B-mode images of the CCA. The proposed method looks for the best smooth curves, according to a new gain function. The smooth curve model is a cubic spline and the search is made efficient by adapting the random sample consensus (RANSAC) algorithm [27] to longitudinal sections of the carotid.

The proposed method presents several attractive features, in particular: it is robust to speckle and irregular contrast; it has the capability of adjusting to flexible tubular shapes; it includes a global smoothness constraint; and the human interaction is minimal. The outline of the paper is as follows. Section 2 presents the dataset and describes the proposed method, including the computation of the complete edge map and the valley edge map using a new non-linear smoothing filter. It also describes the detection of the carotid adventitia in longitudinal sections of the CCA using RANSAC and cubic splines. The parameter settings and illustrating results are presented in Section 3. Results are discussed in Section 4. Conclusions and topics for future research are given in Section 5.

2.   Materials and methods

2.1.   Dataset

A set of 50 longitudinal B-mode images of the CCA was acquired with a Philips HDI 5000 ultrasound system and recorded with 256 gray levels. Seven of these images include a part of the internal carotid artery. The image pixel size was normalized to 0.09 mm, a common value used in clinical practice. The parameter settings of the scanner were not kept the same for every image since we aimed at achieving robustness to different settings.

The image dataset was taken from 25 different symptomatic subjects, 14 of which were males. Plaques of several classes (class II to class IV), sizes and shapes were found in 20 subjects. In order to minimize the correlation between images, only isolated frames of different scans were recorded. All images were manually segmented by two medical experts, A and B. One year after, expert A repeated the manual segmen-

tation, in order to estimate the intra-observer error. Hereafter, the manual segmentations of expert A and expert B and the automatic segmentations will be referred to as MA1, MA2, MB1 and A, respectively.

The manual segmentation of each image consisted of the delineation of the innermost boundaries of the adventitia and the intima regions, at the NE and the FE carotid walls.

The selection of the dataset was based on the ability of medical doctors to make at least a rough outline of the intima-media region boundaries, in the B-mode image, without any complementary information like power Doppler imaging. The sample includes cases with boundary gaps, where the location of the boundary had to be inferred.

2.2.   Overview of the approach

The proposed approach is illustrated in the block diagram of Fig. 1(a), showing the processing flow applied to the input B-mode image of the CCA (Fig. 1(b)). The final result is an estimate of the NE and FE adventitia boundaries (Fig. 1(g)). The
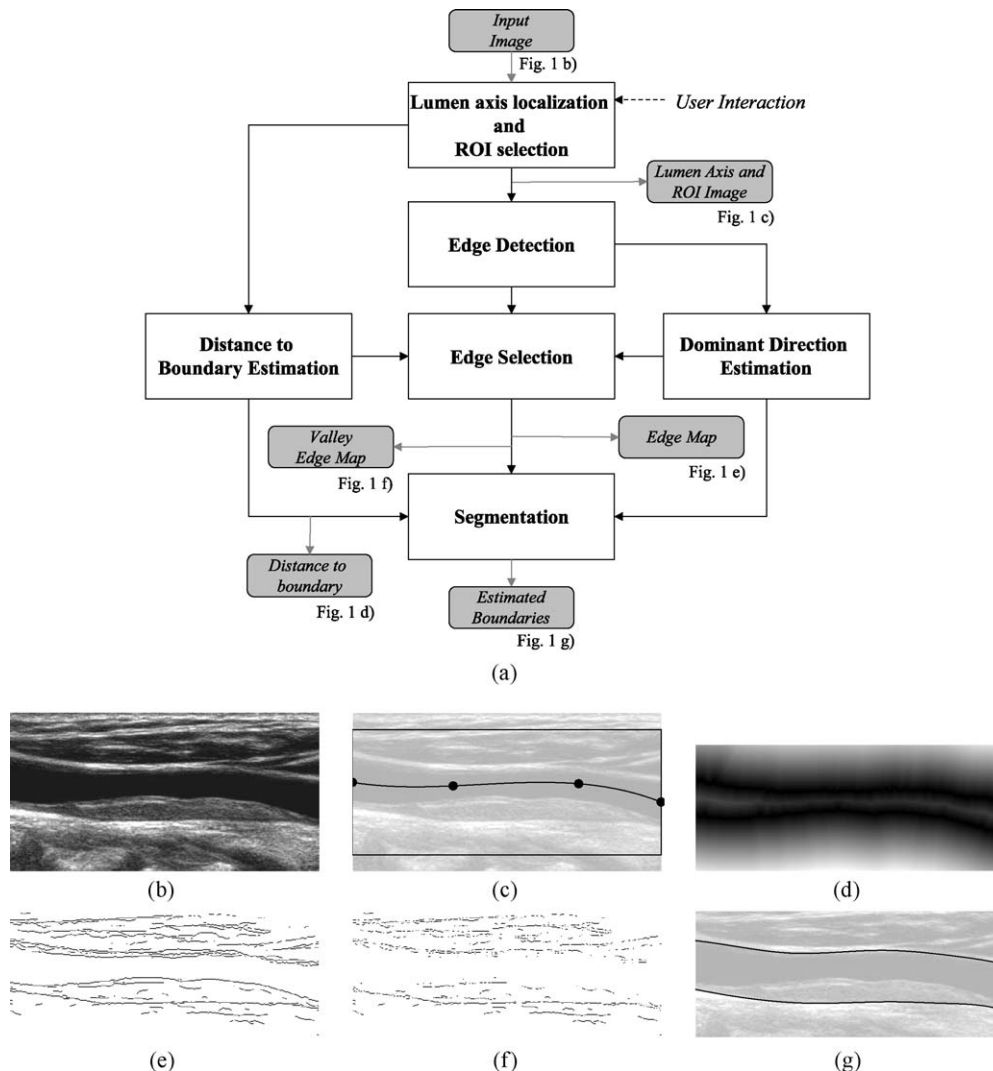
Fig. 1 – Main steps of the method: (a) block diagram; (b) input image; (c) points entered by the user, the interpolated lumen medial axis and the ROI (region inside the rectangle); (d) the absolute values of SDL, |SDL|; (e) edge map; (f) valley edge map; (g) estimated adventitia boundaries.

user starts by defining at least two points close to the lumen medial axis, one at each extremity of the longitudinal axis. If the axis is significantly bended, then one or two additional points should be entered (Fig. 1(c)). This is the only human interaction required and it can be replaced by an automated procedure [28]. An estimate of the lumen axis is obtained by cubic spline interpolation.

The region of interest (ROI) is chosen as the smallest rectangular box containing all pixels within a distance d_{max} to the interpolated lumen axis (Fig. 1(c)). This distance can be estimated from the largest carotid found in a dataset.

The signed distance to the lumen boundaries (SDL) is the distance map to the carotid lumen boundaries, having negative values inside the lumen region. Fig. 1(d) shows the absolute values of SDL, |SDL|, represented as an intensity map. The SDL is determined from a rough estimate of the lumen region, which can be obtained by thresholding using the basic triangle thresholding algorithm described in [29].

The edges inside the ROI are detected using a new non-linear image filter, non-maximum suppression and hysteresis. To reduce the error in the gradient direction at edges, the local dominant gradient direction is estimated. It is used, together with SDL and d_{max}, to select the edges of interest that define the final edge map (Fig. 1(e)). The valley edge map is a subset of that map containing the edges with a valley shaped intensity profile (Fig. 1(f)).

The segmentation block takes the SDL, the dominant gradient direction map, the edge map and the valley edge map as inputs, to estimate the NE and the FE adventitia boundaries (Fig. 1(g)) using RANSAC and cubic splines.

2.3. Edge estimation

The main goal of the edge estimation step is to obtain a map of pixels whose properties, such as edge magnitude, gradient orientation and valley shaped intensity profile, are compatible with the adventitia boundaries. The estimation of edges can be divided into the following main steps: edge detection (Section 2.3.1), estimation of the dominant gradient direction at edges (Section 2.3.2), selection of the edges of interest that define the final edge map (Section 2.3.3) and determination of the valley edge map (Section 2.3.4).

2.3.1. Edge detection
To obtain a low noise edge map and good edge localization, a new smoothing filter was conceived and applied to the ROI. The proposed filter was inspired in Tauber's anisotropic diffusion model for ultrasound images [30], which takes advantage of the instantaneous coefficient of variation (ICOV) edge detector [31,32], since it performs better in images with speckle than classical edge detectors, conceived for additive noise. The ICOV value at pixel (i, j) is given by:

$$ICOV(x,y) = \sqrt{\frac{|(1/2)||\nabla I(x,y)||^2 - (1/16)(\nabla^2 I(x,y))^2|}{(I(x,y) + (1/4)\nabla^2 I(x,y))^2}} \quad (1)$$

where I represents the image intensity, $||\nabla I(x,y)||^2 = 0.5[||\nabla_- I(x,y)||^2 + ||\nabla_+ I(x,y)||^2]$, $\nabla_- I(x,y) = (I(x,y) - I(x-1,y), I(x,y) - I(x,y-1))$, $\nabla_+ I(x,y) = (I(x+1,y) - I(x,y), I(x,y +$

$1) - I(x,y))$, $\nabla^2 I(x,y) = I(x+1,y) + I(x-1,y) + I(x,y+1) + I(x,y-1) - 4I(x,y)$ and $||(u,v)|| = \sqrt{u^2 + v^2}$ is the norm of a vector (u,v).

It is expected that most of the pixels will belong to homogeneous regions and will have low ICOV values, whilst boundaries will appear as outliers, with large ICOV values. Therefore, Tauber's filter uses robust statistics to decide where diffusion should take place and where it should be inhibited. The diffusion coefficient at pixel (x, y) and time t is a Tukey's function [33], given by

$$c(x,y;t) = \begin{cases} \frac{1}{2}\left[1 - \left(\frac{ICOV(x,y;t)}{\sigma_s(t)}\right)^2\right]^2 & ICOV < \sigma_s \\ 0 & ICOV \geq \sigma_s \end{cases} \quad (2)$$

where $\sigma_s = \sqrt{5}\sigma_e$ and σ_e is the image edge scale, estimated with tools from robust statistics based on the ICOV's median absolute deviation (MAD) [30,33]. It is computed as [30]

$$\sigma_e = CMAD(ICOV) + \underset{\Omega}{med}(ICOV)$$

$$= C\underset{\Omega}{med}|ICOV - \underset{\Omega}{med}(ICOV)| + \underset{\Omega}{med}(ICOV) \quad (3)$$

where $\underset{\Omega}{med}(r)$ is the median of r over the image domain, Ω, and $C = 1.4826$ is a constant.

Despite of its advantages, Tauber's model has the drawback of destroying some important anatomical boundaries when they have low contrast at bright regions, where the ICOV is weak. An example of this problem can be seen in Fig. 2(c), where the weak valley edge pointed by the arrow inside the circle was destroyed. To overcome this problem, we borrowed concepts from the total variation theory [34,35] and embedded the curvature information in a new model, given by

$$\begin{cases} \frac{\partial I(x,y;t)}{\partial t} = c(x,y;t)\kappa(x,y;t)||\nabla I(x,y;t)|| \\ I(x,y;0) = I_0(x,y) \\ \frac{\partial I(x,y;t)}{\partial \vec{n}} = 0 \quad \forall (x,y) \in \partial\Omega \end{cases} \quad (4)$$

where $c(x,y;t)$ is the Tukey's function given by Eq. (2), ∇I is the intensity gradient, I_0 is the initial image, at time $t = 0$, $\partial\Omega$ is the image boundary and $\vec{n}$ is the outward normal at the image boundary. $\kappa(x,y)$ is the mean curvature, updated at each time step, given by

$$\kappa(x,y) = div\left(\frac{\nabla I(x,y)}{||\nabla I(x,y)||}\right) \quad (5)$$

With this new model, the diffusion is inhibited not only at places where the ICOV is high, as in Tauber's model, but also where the curvature is small, as is usually expected for anatomical structures. On the other hand, the noise is strongly smoothed out because it usually has high curvature and low ICOV. As can be seen in Fig. 2(e), our filter produces well localized edges and is also able to preserve important anatomical boundaries that are destroyed by Tauber's filter.
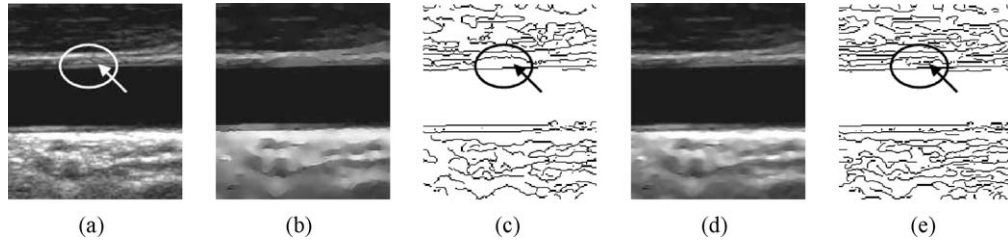
Fig. 2 – Edge maps produced by non-linear filtering: (a) a longitudinal section of a CCA and weak valley edges pointed by an arrow; (b) smoothed image obtained with Tauber's filter; (c) edge map of image (b) showing erosion of weak valley edges; (d) smoothed image obtained with our filter; (e) edge map of image (d) showing a better preservation of weak valley edges.

The edge map is built from the smoothed ROI produced by the new filter, using the ICOV to measure the edge strength and non-maxima suppression and hysteresis [36] to select the strongest edges. Hysteresis requires two thresholds for the ICOV, T_1 and $T_2 < T_1$. The first threshold is set to $T_1 = \sigma_e$, where σ_e is computed using Eq. (3) and the smoothed image produced by the new non-linear filter. A good range for the second threshold is $T_1/3 < T_2 < T_1/2$ [36]. Therefore, it was set to $T_2 = 0.4T_1$. Finally, the edge map is processed by morphological thinning [37], to make sure the contour edges are one pixel thick.

2.3.2. Dominant gradient direction

In B-mode images, large errors are expected in the gradient orientation due to noise and image artifacts. Gradient orientation errors are reduced by computing the local dominant gradient direction, at each pixel. Let $\nabla I_{i,j}^n$ be the intensity gradient at pixel (i,j), in iteration n, and ∇I_k^{n-1} the gradient at the k th pixel in the 8-neighborhood of (i,j), in iteration $n-1$. We compute $\nabla I_{i,j}^n$ as the average of ∇I_k^{n-1}, for $k = 1, 2, \ldots, 9$, considering only the neighbors whose gradient makes an angle less than $45°$ with the gradient at the central pixel, to avoid the interference of close contours with very different orientations.

Since the edge detection depends on the gradient orientation, a small fraction of the edges in iteration zero may disappear and new ones may arise as the gradient orientation changes along iterations. Nevertheless, that edge map is a good estimate of the final edge map and it can be used as a representative sample of the edge population. Therefore, we use its edge pixels as a reference to evaluate the stability of the gradient orientation.

In the evaluation of the stopping criterion, the edge points whose gradient orientation does not stabilize along iterations
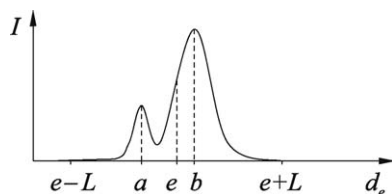
Fig. 3 – Typical intensity profile of a valley edge, where: I is the intensity, e is the location of the edge, d_e is the distance from the edge in the direction of its intensity gradient, $\nabla I(e)$, a is the location of the lower peak, b is the location of the higher peak, and L is the maximum distance of search.

should be considered outliers. Let α be the random variable representing the angle change in the gradient orientation between consecutive iterations, at each edge of the initial edge map. It is known, from robust statistics, that $\sigma_\alpha = \text{CMAD}(\alpha) + \text{med}(\alpha)$ gives a good estimate of the threshold at which the outliers start to appear [30]. To get a robust estimate of the threshold, σ_α^*, above which no inliers are expected, we appeal to Tukey's error norm and set $\sigma_\alpha^* = \sqrt{5}\sigma_\alpha$ [33]. Iterations are stopped when the value of α is less than a small angle, ϵ, for all inliers. In other words, they are stopped when $\sigma_\alpha^* < \epsilon$. We set $\epsilon = 0.1°$, to guarantee a good stability to all inliers.

2.3.3. Edge selection

In order to reduce the computational cost and the chances of the automatic contour being attracted to other edges, the final edge map (Fig. 1(e)) only keeps the edges that are compatible with the adventitia boundaries. The selection of these edges is based on their gradient orientation, their distance to the lumen axis and their SDL value.

Since the adventitia region is brighter than the intima-media region, all edges with gradient pointing to the interior of the artery should be neglected. Let $\gamma(i,j)$ be the angle, at a given pixel, (i,j), between the intensity gradient and the gradient of the distance map to the estimated medial axis. Being $\gamma_{\max}$ the threshold above which the probability of finding an edge of the carotid adventitia is virtually zero, all edge pixels for which $\gamma(i,j) > \gamma_{\max}$ can be removed from the edge map.

All edges in the ROI whose distance to the lumen axis is larger than a certain threshold, $d_{\max}$, or such that $\text{SDL}_{\min} < \text{SDL} < \text{SDL}_{\max}$ are also removed from the edge map.

The determination of $\gamma_{\max}$, $d_{\max}$ and the two SDL thresholds will be discussed in Section 3.1.

2.3.4. Valley edge map

One of the discriminating features of the carotid adventitia is its valley-shaped intensity profile (Fig. 3), called 'double line' pattern [12].

The valley edge map (Fig. 1(f)) is a subset of the edge map (Fig. 1(e)) obtained after the edge selection described above. The determination of the valley edge map begins with a search, up to a certain distance, L, for the first local intensity maximum (Fig. 3) in both directions along the line defined by each edge point, e, and the corresponding intensity gradient, $\nabla I(e)$. The intensity profile of a valley edge has two intensity peaks, at locations a and b, being one of these usually lower. Due to noise, other edges can also have a double peak
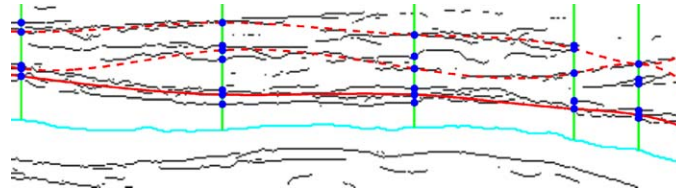
Fig. 4 – Boundary sampling: upper part of the edge map of Fig. 1(e), showing a sample of abscissas (green lines) above the lumen axis (cian curve), the corresponding edges (blue points), two bad splines (dashed red curves) and the best spline (solid red curve).

intensity profile, but their lower peak will be weak. Therefore, all profiles with only one peak or a weak lower peak should not be classified as valley edges. To detect the strong lower peaks, an approach similar to the edge detection scheme described at the end of Section 2.3.1 can be used. Using hysteresis and assuming that A is a random variable representing the amplitude of the lower peak, the high threshold can be set to $T_A = \text{CMAD}(A) + \text{med}(A)$ and the low threshold to $0.4T_A$. However, experimentation showed that using only the lower threshold is better because it captures more valley edges without a significant increase in noise. Therefore, an edge pixel is classified as a valley edge if $A > 0.4T_A$.

2.4.   Segmentation of the adventitia using RANSAC

The proposed method for the segmentation of the adventitia boundary is based on a RANSAC search of the best fit of a given contour model according to a specified cost function. The RANSAC algorithm allows for the estimation of model parameters from a data set containing a large number of outliers. It works by repeatedly extracting a random sample, with the minimum number of data points required to determine the model parameters. The consensus of the model is then evaluated for the rest of the population and the model with the best consensus is selected. The process is terminated when there is a high confidence in having drawn at least one good sample.

The method proposed in this paper assumes a cubic spline [38] as a model for the adventitia boundary because, unlike other splines, it gives smooth curves, it is relatively easy to implement and it offers a stable behavior. Moreover, the results showed that it is able to adequately follow the CCA adventitia in longitudinal sections. A specialized gain function is used to evaluate the spline consensus. Samples of image abscissas are drawn and used to generate the samples of spline control points (sets of edge pixels with different abscissas) needed to determine the spline parameters. The search for the best fit stops when the number of drawn samples exceeds an automatically determined threshold. A detailed discussion of these issues will be presented next.

2.4.1.   Sample generation and the adventitia model
The sample generation uses *a priori* knowledge of the distribution of the inliers. In longitudinal sections of the CCA, samples must have different abscissas. Therefore, a set of n different abscissas is randomly drawn and used to determine n vertical lines above and below the lumen axis, separately, as illustrated

in Fig. 4. Good abscissas are those for which the corresponding vertical line contains a good point, that is an edge point of the carotid boundary.

Fig. 4 illustrates the search for the NE adventitia. A spline is built from each sample of n edge points with different abscissas. Usually there are several edge points for each abscissa. The algorithm evaluates all the splines fitted to the samples of n edge points for each sample of n abscissas and selects the best spline according to a predefined criterion. A similar procedure is used for the segmentation of the FE adventitia. Setting $n = 5$ corresponds to the use of 4 cubic polynomials which is enough to give some flexibility to the model without compromising its robustness to noise.

The determination of the spline parameters relies on the orientation of the intensity gradient at the end points, requiring a good degree of confidence in the gradient orientation at each edge point. This confidence is achieved through the estimation of the local dominant direction of the gradient, as described in Section 2.3.2.

2.4.2.   Model consensus
The consensus of the fitted spline is measured by a gain function integrating the response to several discriminating features of the carotid boundaries.

One good discriminating feature is the valley shaped edge property, already explored in previous works on the segmentation of the CCA [16,18]. However, these valley edges are often missing in large extensions of the CCA adventitia and can also be found in other anatomical structures surrounding the CCA, frequently having lower edge strength than other boundaries. Thus, a good model should be supported by additional features. First, it should look for any type of edges, giving more emphasis to valley edges and edges closer to the detected lumen boundary. Second, a larger absolute value of the SDL (signed distance to the lumen boundary) should receive a stronger penalty, in order to reduce the influence of other anatomical boundaries. However, due to the eventual presence of plaque, this penalty should have a slower growth for positive distances (those outside the lumen). Third, there should be a good orientation consistency between the normal to the carotid adventitia model and the intensity gradient. These observations led to a gain function that integrates the responses to the following features:

1. distance of the carotid adventitia model to any edge points, de;

2. distance to valley edge points, *dve*;
3. angle, θ, between the orientation of the normal to the adventitia model and the intensity gradient;
4. signed distance to the lumen boundary, SDL.

The way these features are integrated into the gain function should reflect the probability of each adventitia model point belonging to the carotid boundary. Bearing in mind that the valley edge property is not always present, an adventitia model point, P_k, has a high probability of belonging to the carotid boundary if it is close to a valley edge *or* a step edge, *and* it has an intensity gradient orientation similar to the orientation of the normal to the adventitia model *and* it falls inside the expected distance limits to the lumen boundaries. Moreover, the chance of each adventitia model point being a good candidate should increase as each feature becomes stronger, reaching the maximum at the best fit. The best adventitia model should be the one with the highest global score for the set of all its points.

Taking all this into consideration, the following gain function was defined:

$$G = \frac{1}{2m} \sum_{k=1}^{m} [g_1(P_k) + g_2(P_k)]\, g_3(P_k) g_4(P_k) \tag{6}$$

where m is the number of P_k points of the digital spline and $g_j(P_k)$, $1 \le j \le 4$, are fuzzy functions representing the contribution of feature j at P_k.

In Eq. (6), $g_1(P_k) = f(de(P_k))$, $g_2(P_k) = f(dve(P_k))$ and $g_3(P_k) = f(\theta(P_k))$, where $f(z)$ is the Tukey's function, given in Eq. (7), with scale $\sigma = \sigma_d$ for features *de* and *dve* and scale $\sigma = \sigma_\theta$ for θ.

$$f(z) = \begin{cases} \left[1 - \left(\dfrac{z}{\sigma}\right)^2\right]^2 & z < \sigma \\[4mm] 0 & z \ge \sigma \end{cases} \tag{7}$$

The scale, σ, of each fuzzy function represents the threshold of the corresponding feature above which adventitia boundary pixels are no longer expected to be found.

Function g_4 gives preference to curves that are closer to the lumen boundary and a larger tolerance to those outside the lumen. This is expressed as

$$g_4(P_k) = \begin{cases} f^-(-\text{SDL}(P_k)) & \text{SDL}(P_k) < 0 \\[2mm] f^+(\text{SDL}(P_k)) & \text{SDL}(P_k) \ge 0 \end{cases} \tag{8}$$

where $f^-(z)$ and $f^+(z)$ are given by Eq. (7), with scales $\sigma = \sigma^-$ and $\sigma = \sigma^+$, respectively.

The shapes of these fuzzy functions are inspired in Tukey's function for several reasons: (a) its success in the field of robust statistics [30]; (b) the existence of a robust estimator, based on the MAD statistic, for the scale of the fuzzy function; (c) its computational lightness.

The gain function has values in the range [0, 1], where unity means a perfect fit. Its score reflects the percentage of good points along the path of the adventitia model and may be viewed as an estimate of the probability of drawing a good abscissa.

The evaluation of the spline consensus has a significant contribution to the total computational effort of the RANSAC algorithm. Therefore, two bail-out tests are used to alleviate this burden. The first one rejects any sample of n abscissas not well spread along the columns of the image, in order to guarantee a good support for the spline model. This restriction can be introduced in a very efficient way by excluding the image column corresponding to the last drawn abscissa and all its neighbor columns, up to a specified distance, Δ, before drawing another abscissa. To get a good spreading of the abscissas in each sample, $\Delta = (m-1)/(2(n+1))$ was chosen, where n is the size of the sample and m is the number of columns in the image. So, if $n = 5$ (4 polynomials) then $\Delta = (m-1)/12$. The second bail-out test rejects any sample of n points if the angle, θ, between the gradient intensity and the spline normal is larger than a threshold σ_θ at any point of the sample. The value of σ_θ will be discussed in Section 3.1. The spline consensus is computed only for samples that are not rejected by the bail-out tests.

To further reduce the computational effort, a digital spline is used in the consensus evaluation because: it is easily obtained by rounding the real-valued spline at each abscissa; no interpolation is needed; and it is enough to find a good estimate of the best spline fit.

2.4.3. Stopping criterion

The minimum number of samples, k, that should be inspected can be determined by adding a few standard-deviations, σ, to the expected number of samples, μ, necessary to get a good sample [39], that is:

$$k > \mu + N\sigma = \omega^{-n} + N\frac{\sqrt{1 - \omega^n}}{\omega^n} \tag{9}$$

where N is the number of standard-deviations added to the mean, n is the size of the sample and ω is the proportion of inliers in the data set.

The proportion of inliers is set to $\omega = P$ ('good abscissa'), a probability that is estimated by the gain function. After the processing of each sample of n abscissas, ω is updated as the highest value found for the gain function, up to that moment. The procedure is terminated when the number, k, of drawn samples of abscissas exceeds the number given by the second member of Eq. (9).

3. Results

3.1. Parameter setting

Since the algorithm depends on a large number of parameters, it would not be possible to evaluate the final output of the method for all parameter combinations. Therefore, parameters were either estimated automatically (σ_e, T_A, etc.) or through experimental tests related to the particular result desired for each parameter. For instance, the ROI size should be as small as possible but large enough to contain the carotid region. Another example is the estimation of $\gamma_{\max}$ (Section 2.3.3) discussed below.

The non-linear smoothing filter (Eq. (4)) was discretized with the numerical scheme proposed in [40]. Two parameters
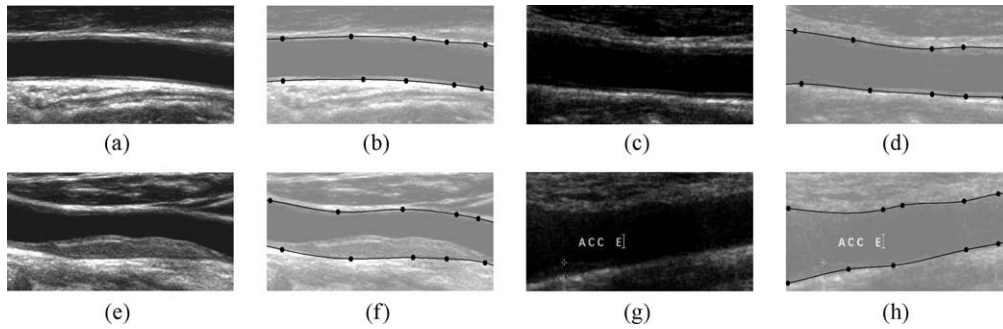
Fig. 5 – Longitudinal B-scans of the CCA and the corresponding faded versions with the best computed splines and their control points.

of this scheme are the image grid size, h, which was normalized to one, and the time step, Δt, that was set to 0.25 in order to obtain a good convergence speed without loosing numerical stability. The value of the edge scale, σ_e (Eq. (3)), as well as the slope of the corresponding curve, decrease monotonously with an increasing number of iterations. The change in σ_e is proportional to the amount of smoothing generated by the previous iteration. Therefore, iterations are stopped when the rate of change of σ_e falls below 5×10^{-4}, after which the smoothing increases very slowly.

The value of N, in Eq. (9), has to give a high confidence in finding a good sample. In literature related to RANSAC (e.g., [39,41]) it is common to select $1/N^2 \approx 0.05$, which gives $N \approx 4.5$. Therefore, $N = 5$ was chosen.

In the used dataset, the distance from a carotid adventitia point to the lumen medial axis is less than 70 pixels. In order to keep some of the image data outside the carotid boundaries, we set $d_{max} = 90$ pixels. This gives a good safety margin for new images. It also minimizes the influence of the boundary conditions of Eq. (4) over the carotid region during image smoothing.

The value of γ (Section 2.3.3) was computed in the neighborhood of the manually traced carotid boundaries, along each image column, for the edge point closest to these boundaries. Some values of γ are outliers, corresponding to noise edges or

belonging to other contours that appear in the same neighborhood. Nevertheless, it was observed that $\gamma < 30°$ in at least 99% of the cases, which means that $\gamma_{max} = 30°$ is an adequate value.

The parameter SDL_{min} represents the threshold of SDL below which no edge pixel of the carotid adventitia is expected to be found. It was observed that $SDL > -6.4$ in every image of the dataset. Therefore, we set $SDL_{min} = -7$ and $\sigma^- = -SDL_{min} = 7$. On the other hand, parameters SDL_{max} and σ^+ represent the threshold of SDL above which no edge pixel of the adventitia is expect to be found. A natural value for this threshold is d_{max}, leading to $SDL_{max} = \sigma^+ = d_{max}$.

The width measurement of the valley edges in the dataset showed that $L = 10$ is enough for valley edges belonging to the adventitia.

To estimate the values of σ_d and σ_θ, the values of de and θ (Section 2.4.2) were computed for each point of the adventitias manually traced by one of the experts (MA1). Parameter θ was computed from the image gradient map, obtained with the local dominant gradient direction filter. Parameter de was computed from the edge map, described in Section 2.3.3. Parameters σ_d and σ_θ are scales of Tukey's functions. Therefore, they can be computed as $\sigma_d = \sqrt{5}\,[\text{CMAD}(de) + \text{med}(de)]$ and $\sigma_\theta = \sqrt{5}\,[\text{CMAD}(\theta) + \text{med}(\theta)]$, respectively, which gives $\sigma_\theta \approx 11°$ and $\sigma_d \approx 4$.
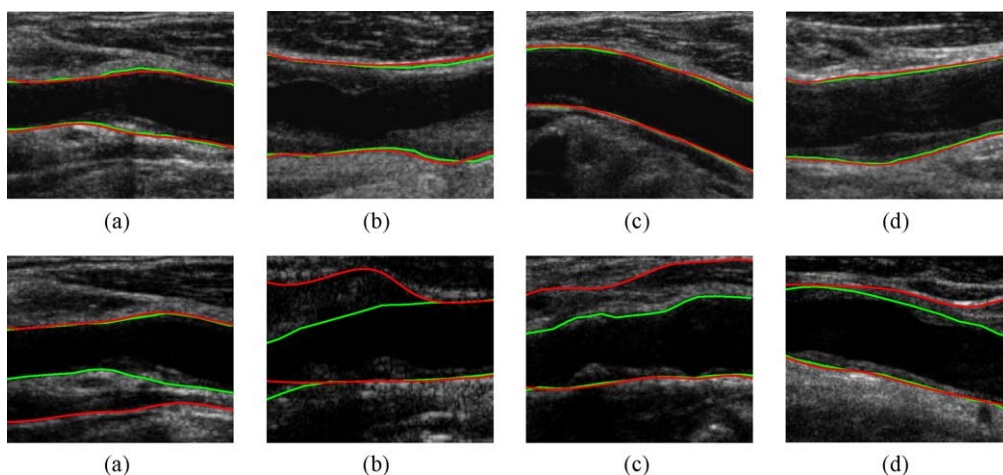
Fig. 6 – Top: Successful adventitia detections. Bottom: Adventitia misdetections. The detected contours are in red and the manually traced ones (MA1) are in green.
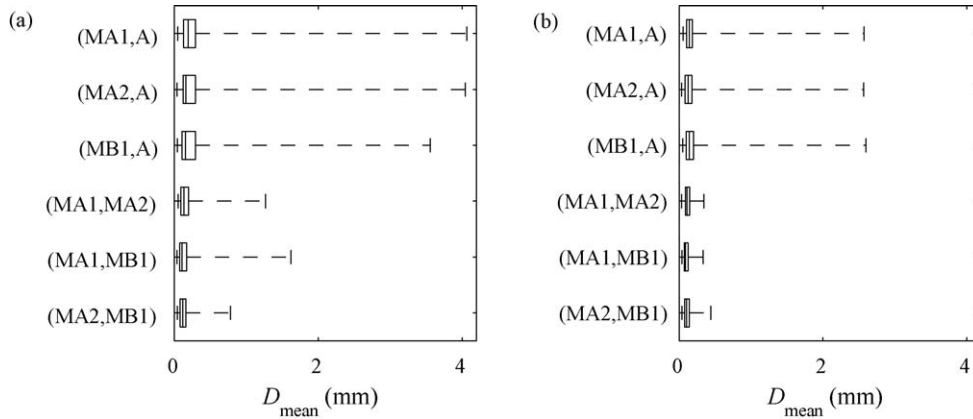
Fig. 7 – D_{mean} statistics for the detected adventitia: (a) NE boundary; (b) FE boundary.

One parameter of the bail-out tests used in the RANSAC algorithm was also determined from the dataset. This parameter is the limit for the angle, θ, between the intensity gradient and the normal to the adventitia model at the sample points. Its value is given by the threshold σ_θ, also used in the gain function as already discussed above.

3.2.   Segmentation examples

Examples of well detected carotid adventitias are presented in Fig. 5, including a case of successful segmentation in the presence of graphical markings placed during the image acquisition (Fig. 5(g) and (h)). The last two B-scans have large plaques. The values of the gain function for the splines above (G_a) and below (G_b) the lumen are: $G_a \approx 74.3\%$ and $G_b \approx 81.6\%$ for Fig. 5(b); $G_a \approx 60.6\%$ and $G_b \approx 69.7\%$ for Fig. 5(d); $G_a \approx 62.0\%$ and $G_b \approx 63.9\%$ for Fig. 5(f); $G_a \approx 49.1\%$ and $G_b \approx 50.7\%$ for Fig. 5(h).

Fig. 6 (top) shows some other examples of successful detections, including three cases with visible large plaques (Fig. 6(a),(b) and (d) (top)). The results are compared with manual contours (MA1). Typical misdetections are given in Fig. 6 (bottom), corresponding to cases where the visibility of the adventitia is quite bad or where its echo is weaker than the echo of other similar boundaries.

3.3.   Statistical analysis

Since the quality of the results depends on the quality of the image set, the best way to evaluate the algorithm is by comparing the automatic contours with the manual contours traced by medical experts. The statistical evaluation was based on the vertical distances between manual and automatic contours along the longitudinal direction.

The following statistics allow a global evaluation of the inter-method and the inter-observer agreement. D_{mean} measures the mean vertical distance between two different contours (manual or automatic) for the same boundary. CD_{mean} and $CDRE_{mean}$ represent, respectively, the mean of the absolute differences and the mean of the relative absolute differences, along the longitudinal axis, between different measures of the carotid diameter. To compute $CDRE_{mean}$, the absolute differences between different diameter measures are divided by the largest manual estimate of the corresponding diameter and averaged for each image. The carotid diameter was computed as the vertical distance between the NE and the FE adventitia contours.

Figs. 7, 8 (top) and Table 1 show the distribution of the D_{mean} statistics. These distributions can be used to assess the inter-method and the inter-observer agreement. In Fig. 7, the box whiskers were set to the smallest and the largest values, while the three vertical lines of the boxes represent the first quartile, the median and the third quartile of the data. Fig. 7 and Table 1 show that, for FE boundaries, $0.09\,mm \leq \text{median}(D_{mean}) \leq 0.11\,mm$ for manual detections and $0.13\,mm \leq \text{median}(D_{mean}) \leq 0.14\,mm$ for automatic ones. For NE boundaries, $0.11\,mm \leq \text{median}(D_{mean}) \leq 0.13\,mm$ for manual detections and $0.15\,mm \leq \text{median}(D_{mean}) \leq 0.19\,mm$ for automatic ones. There is a slightly larger dispersion of D_{mean} values for automatic detections, except for misdetection cases, corresponding to the largest values of D_{mean}. Fig. 8 (top) gives the cumulative distribution of D_{mean}, showing the percentage of images for which this statistic falls below a

Table 1 – D_{mean} statistics for the detected NE and FE adventitia.

| | | D_{mean} (mm) | | |
		Lower quartile	Median	Upper quartile
(MA1,A)	NE	0.13	0.19	0.29
	FE	0.10	0.14	0.19
(MA2,A)	NE	0.12	0.16	0.29
	FE	0.08	0.13	0.18
(MB1,A)	NE	0.10	0.15	0.29
	FE	0.10	0.14	0.20
(MA1,MA2)	NE	0.09	0.13	0.20
	FE	0.09	0.11	0.15
(MA1,MB1)	NE	0.07	0.11	0.17
	FE	0.07	0.09	0.13
(MA2,MB1)	NE	0.08	0.12	0.16
	FE	0.08	0.11	0.14
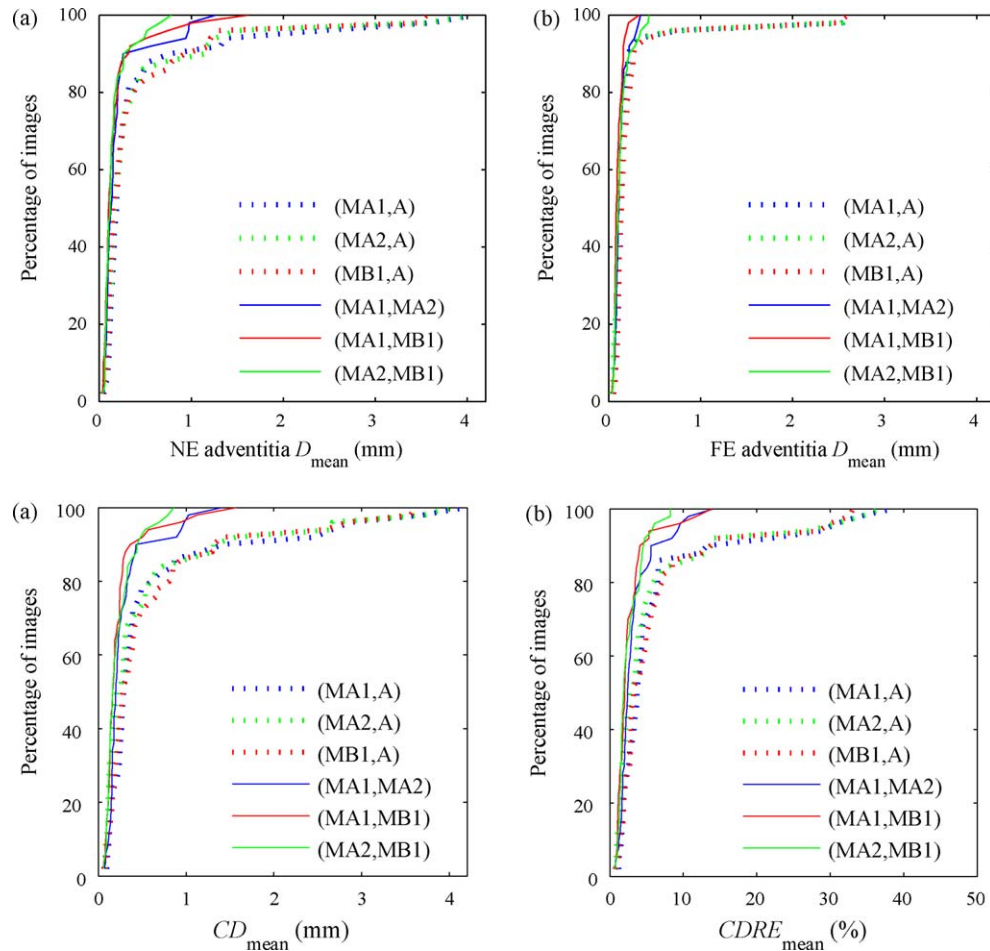
Fig. 8 – Top: D_{mean} cumulative distribution for the detected adventitia: (a) NE boundary; (b) FE boundary. Bottom: Cumulative distributions for the estimated carotid diameter: (a) CD_{mean}; (b) $CDRE_{mean}$.

given value. The cumulative distribution curves of the D_{mean} for manual and automatic contours differ less than one pixel (0.09 mm) in approximately 73% of the NE boundaries and in approximately 95% of the FE boundaries.

As shown in Fig. 8 (bottom), CD_{mean} curves for automatic detections differ from the manual versions less than two pixels (0.18 mm) in approximately 70% of the images. For this percentage, the $CDRE_{mean}$ cumulative distribution curves for manual and automatic segmentations differ less than 2.5%.

Bland–Altman plots [42] and the estimated mean diameter of the carotid, $DIAM_{mean}$, were also used to assess the agreement between methods and between observers. Figs. 7 and 8 (top) show that some of the automatic detections can be seen as outliers, since they correspond to misdetections and have a much larger value of D_{mean} than most of the other detections. In order to reduce the influence of these outliers, the Bland–Altman plots were computed only for the best 75% automatic detections of both NE and FE boundaries. Fig. 9 shows these plots for the differences between $DIAM_{mean}$ values of two given methods against their average, as well as the limits of agreement in the form Mean ± 2SD mm, where SD is the standard deviation. The results show that -0.13 mm $\leq$ Mean ≤ 0.14 mm for manual contours and 0.09 mm $\leq$ Mean ≤ 0.23 mm for the automatic detections. The

worst limits for [Mean − 2SD,Mean + 2SD] mm are [−0.49, 0.58] for manual contours and [−0.31, 0.58] for automatic ones.

The method was implemented in Matlab, on a PC equipped with an Intel Core 2 Duo processor at 2.13 GHz and a 2 GB RAM. The median CPU time per image spent in the main tasks of the adventitia detection was: 2.8 s in the image smoothing; 9.9 s in the estimation of the dominant gradient direction; 4.8 s in the RANSAC search. The median total time was 28.5 s.

4. Discussion

Fig. 7, Table 1 and Fig. 8 (top) show that different manual tracings of a given carotid boundary can differ more that 1 mm in some of the images, which is an evidence of the difficulty that an expert has in locating these contours. This is due to the poor definition and ambiguity of the true location of the adventitia contours. It should also be mentioned that several images in the dataset include a large part of the internal carotid, a region that is more difficult to segment than the CCA.

The good detection of the FE adventitia in Fig. 5(f) illustrates the robustness of the algorithm to the presence of large plaques. The value of the gain function obtained for the lower spline (Section 3.2) is an example of an underestimated proba-
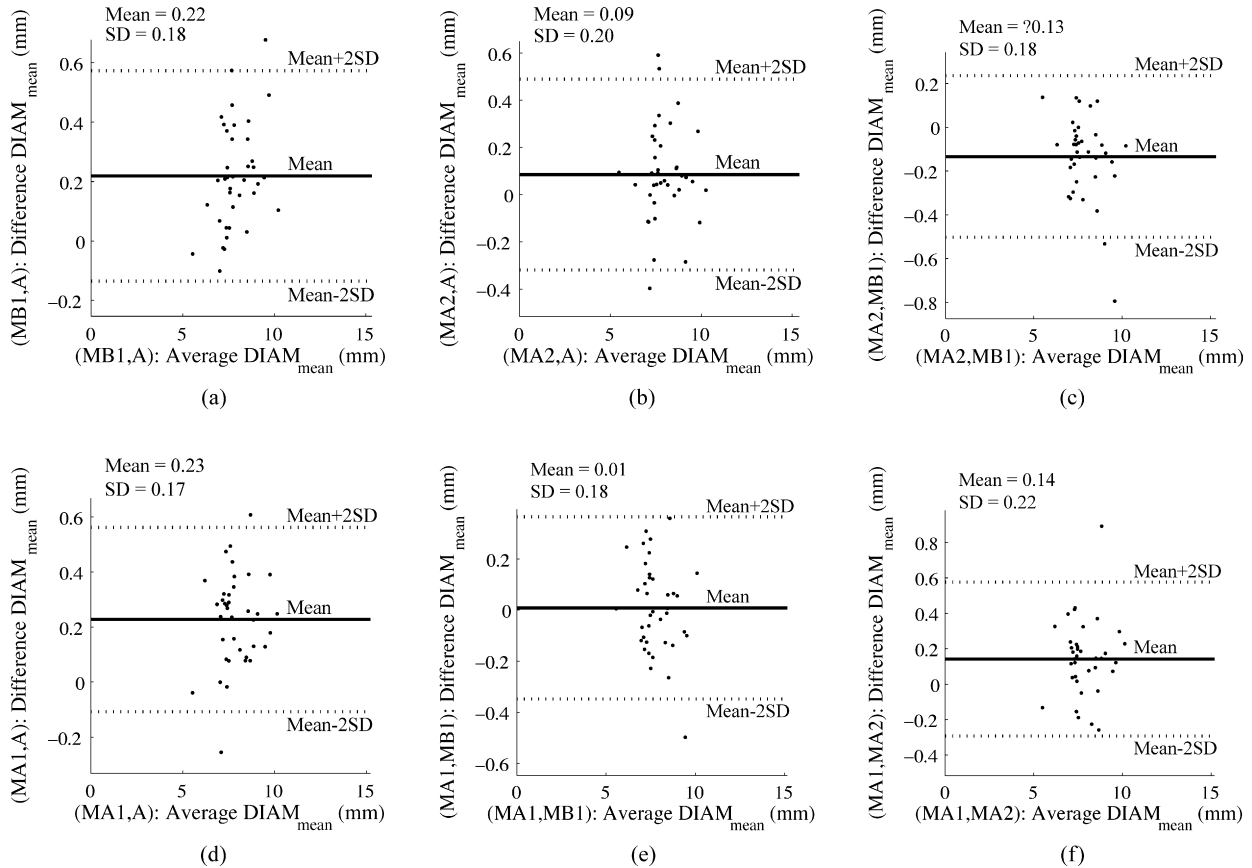
Fig. 9 – Bland–Altman plots of $DIAM_{mean}$, where SD represents the standard deviation.

bility of a good abscissa due to the influence of a thick plaque. In this case, the plaque region pushes the lumen boundary away from the adventitia boundary, reducing the value of the SDL factor (g_4) in the gain function. A consequence of this underestimation is an increase in the number of samples analysed by the RANSAC algorithm, which means an increased confidence on the fitted adventitia model, at the cost of some additional computational effort. However, the quality of the segmentation is not affected. The increase in D_{mean} for the automatic FE adventitia is less than 0.24 pixels (0.0216 mm) when compared to manual tracings. A large valley structure is also visible at the upper boundary of the plaque, but this feature has a much stronger presence along the lower wall boundary.

Misdetections of the carotid adventitia, like those presented in Fig. 6 (bottom), may occur if there are other boundaries that are stronger than the adventitia boundaries and have similar properties, specially when the adventitia is badly defined over a large fraction of its length. Fig. 6a (top) and Fig. 6a (bottom) show two similar images where the competition between the correct boundary and the incorrect one is very tight, leading to a good detection in the first case and to a misdetection in the second one. Although this type of error does not often occur, it is important due to inter-subject variability and it suggests that more information should be added to the cost function, as discussed below.

The results for the manual contours presented in Table 1 (0.09 mm $\leq$ median(D_{mean}) $\leq$ 0.11 mm for FE and 0.11 mm $\leq$

median(D_{mean}) $\leq$ 0.13 mm for NE) show that experienced medical doctors have more difficulty in determining the correct location of the NE adventitia. This is caused by the poorer visibility of NE boundaries, a well known limitation of this image modality that explains the preference for the FE wall in clinical practice, when it comes to the IMT measurement. As in the case of manual tracings, the performance of the proposed algorithm is worse at the NE boundary (0.13 mm $\leq$ median(D_{mean}) $\leq$ 0.14 mm for FE and 0.15 mm $\leq$ median(D_{mean}) $\leq$ 0.19 mm for NE). This difference in the performance is also evident in Fig. 8 (top), where the cumulative distribution of the D_{mean} statistic for manual and automatic contours differ less than one pixel (0.09 mm) in approximately 73% of NE boundaries and in approximately 95% of FE ones. Despite a slightly larger dispersion of D_{mean} values for automatic detections (except for misdetections), our algorithm can correctly detect most of the adventitia boundaries, specially in the FE case. Since FE boundaries are the most frequently used in clinical practice, these results suggest that, if the lumen-intima boundary is also detected, the proposed algorithm could be of great utility for IMT measurements.

Since the estimates of the carotid diameter integrate the errors in the two boundaries, the behavior of CD_{mean} and $CDRE_{mean}$ should be close but inferior to the one observed for NE boundaries. This is confirmed in Fig. 8 (bottom), where the difference between automatic and manual curves becomes significant ($CD_{mean} > 0.18$ mm and $CDRE_{mean} > 2.5\%$) after the 70 percentile.

The Bland–Altman plots of $DIAM_{mean}$ (Fig. 9) indicate a good agreement between the automatic and the manual estimates of the mean carotid diameter. The range of mean differences for automatic detections ($-0.13\,mm \leq$ Mean $\leq 0.14\,mm$) is consistent with the range of mean differences obtained for the automatic detections ($0.09\,mm \leq$ Mean $\leq 0.23\,mm$). The agreement between manual and automatic measures is also confirmed by the analysis of the worst limits of agreement ($[-0.49, 0.58]\,mm$ for manual detections and $[-0.31, 0.58]\,mm$ for automatic ones).

The proposed approach shows promising results and has the potential to further reduce the segmentation errors since more information about the artery can be introduced in the cost function. For instance, false edges can be penalized by analysing the image intensity profile and the spatial distribution of edges found between pairs of edges that are candidates to adventitia edges. This would improve the discrimination between the adventitia boundaries and other boundaries in the image, giving better detection results for both NE and FE boundaries and avoiding errors like the one illustrated in Fig. 6a (bottom).

5. Conclusions

A new algorithm has been introduced for the automatic segmentation of the NE and the FE adventitia boundary in longitudinal B-mode images of the CCA. This algorithm looks for the best smooth global path in the image, according to a novel gain function which integrates the response to several discriminating features of the carotid adventitia. Our implementation of the RANSAC algorithm makes the search for the best path more efficient than its usual implementation. Cubic splines with five control points proved to be good geometric model priors for the carotid adventitia, in longitudinal sections of the CCA. Misdetections were caused by the attraction of the spline to other boundaries with stronger edges, not because the model was inadequate.

Several examples and quantitative evaluations showed that the proposed approach is robust to highly degrading factors, like heavy noise, graphical markings placed during acquisition, missing data and occlusions of the lumen region by plaque, producing estimates of the adventitia boundaries comparable to the contours manually traced by two medical experts. A good performance was observed for the segmentation of the FE adventitia, which is the most frequently used in clinical practice for IMT measurements. As in the detection by medical experts, the automatic detection of the NE adventitia was not so good, mainly due to the usual poor visibility of this boundary in B-mode images of the carotid, although the presence of other anatomical boundaries may also contribute to misdetections.

Some interesting issues deserve to be pursued in the future. The algorithm could be completely automated by making an automatic detection of the lumen axis using an approach like the one proposed in [28]. Another issue is the quantitative evaluation of the proposed non-linear smoothing filter and its quantitative comparison with alternative filters. Finally, adventitia segmentation errors could be reduced by adding more information to the cost function, like information derived from the image intensity profile and the spatial distribution of edges between NE and FE adventitia boundaries.

Conflict of interest

None.

REFERENCES

[1] D. Baldassarre, M. Amato, A. Bondioli, C.R. Sirtori, E. Tremoli, Carotid artery intima-media thickness measured by ultrasonography in normal clinical practice correlates well with atherosclerosis risk factors, Stroke 31 (2000) 2426–2430.

[2] D. O'Leary, J. Polak, R. Kronmal, T. Manolio, G. Burke, S. W. Jr., Carotid-artery intima and media thickness as a risk factor for myocardial infarction and stroke in older adults, N. Engl. J. Med. 340 (1999) 14–22.

[3] H. Hodis, W. Mack, L. LaBree, R. Selzer, C. Liu, C. Liu, S. Azen, The role of carotid arterial intima-media thickness in predicting clinical coronary events, Ann. Intern. Med. 128 (4) (1998) 262–269.

[4] R.S. Reneman, J.M. Meinders, A.P.G. Hoeks, Non-invasive ultrasound in arterial wall dynamics in humans: what have we learned and what remains to be solved, Eur. Heart J. 26 (2005) 960–966.

[5] A. Gee, R. Prager, G. Treece, L. Berman, Engineering a freehand 3D ultrasound system, Pattern Recogn. Lett. 24 (4–5) (2003) 757–777.

[6] M. Sonka, W. Liang, R. Stefancik, A. Stolpen, Handbook of Medical Imaging: Medical Image Processing and Analysis, vol. 2, SPIE, 2000.

[7] G.D. Giannoglou, Y.S. Chatzizisis, V. Koutkias, I. Kompatsiaris, M. Papadogiorgaki, V. Mezaris, E. Parissi, P. Diamantopoulos, M.G. Strintzis, N. Maglaveras, G.E. Parcharidis, G.E. Louridas, A novel active contour model for fully automated segmentation of intravascular ultrasound images: in vivo validation in human coronary arteries, Comput. Biol. Med. 37 (9) (2008) 1292–1302.

[8] A. Tsai, A.J. Yezzi, W.M. W. III, C. Tempany, D. Tucker, A. Fan, W.E.L. Grimson, A.S. Willsky, A shape-based approach to the segmentation of medical imagery using level sets, IEEE Trans. Med. Imaging 22 (2) (2003) 137–154.

[9] D. Cremers, T. Kohlberger, C. Schnorr, Nonlinear shape statistics in Mumford–Shah based segmentation, in: Proc. European Conf. on Computer Vision (ECCV'2002), vol. 2351, Springer LNCS, 2002, pp. 93–108.

[10] D. Cremers, N. Sochen, C. Schnorr, Towards recognition-based variational segmentation using shape priors and dynamic labeling, in: Proc. European Conf. on Computer Vision (ECCV'2003), vol. 2695, Springer LNCS, 2003, pp. 388–400.

[11] D. Cremers, S. Osher, S. Soatto, Kernel density estimation and intrinsic alignment for knowledge-driven segmentation: teaching level sets to walk, Pattern Recognit. 3175 (2004) 36–44.

[12] M. Halenka, Noninvasive measurement of early atherosclerosis by high-resolution B-mode ultrasonography, Acta-Universitatis Palackianae Olomucensis Facultatis Medicae 142 (1999) 7–12.

[13] P.J. Touboul, P. Prati, P.-Y. Scarabin, V. Adrai, E. Thibout, P. Ducimetiere, Use of monitoring software to improve the measurement of carotid wall thickness by B-mode imaging, J. Hypertension 10 (5) (1992) 37–41.

[14] J. Gariepy, M. Massonneau, J. Levenson, D. Heudes, A. Simon, the Groupe de Prevention Cardio-vasculaire en Medecine du Travail, Evidence for in vivo carotid and femoral wall thickness in human hypertension, J. Hypertension 22 (1) (1993) 111–118.

[15] R.H. Selzer, H.N. Hodis, H. Kwong-Fu, W.J. Mack, P.L. Lee, C.R. Liu, C.H. Liu, Evaluation of computerized edge tracking for quantifying intima-media thickness of the common carotid artery from B-mode ultrasound images, Atherosclerosis 111 (1994) 1–11.

[16] T. Gustavsson, Q. Liang, I. Wendelhag, J. Wikstrand, A dynamic programming procedure for automated ultrasonic measurement of the carotid artery, Comput. Cardiol. (1994) 297–300.

[17] R.J. Kozick, Detecting interfaces on ultrasound images of the carotid artery by dynamic programming, SPIE 2666 (1996) 233–241.

[18] T. Gustavsson, R. Abu-Gharbieh, G. Hamarneh, Q. Liang, Implementation and comparison of four different boundary detection algorithms for quantitative ultrasonic measurements of the human carotid artery, Comput. Cardiol. (1997) 69–72.

[19] P. Detmer, G. Bashein, R. Martin, Matched filter identification of left-ventricle endocardial borders in transesophageal echocardiograms, IEEE Trans. Med. Imaging 9 (4) (1990) 396–404.

[20] Q. Liang, I. Wendelhag, J. Wikstrand, T. Gustavsson, A multiscale dynamic programming procedure for boundary detection in ultrasound artery images, IEEE Trans. Med. Imaging 19 (2) (2000) 127–142.

[21] A. Schmidt-Trucksass, D. Cheng, M. Sandrock, J. Schulte-Monting, R. Rauramaa, M. Huonker, H. Burkhardt, Computerized analysing system using the active contour in ultrasound measurement of carotid artery intima-media thickness, Clin. Physiol. 5 (2001) 561–569.

[22] D. Cheng, A. Schmidt-Trucksass, K. Cheng, M. Sandrock, Q. Pu, H. Burkhardt, Automatic detection of the intimal and the adventitial layers of the common carotid artery wall in ultrasound B-mode images using snakes, in: Int. Conf. on Image Analysis and Processing, B. Werner, 1999, pp. 452–457.

[23] D. Cheng, A. Schmidt-Trucksass, K. Cheng, H. Burkhardt, Using snakes to detect the intimal and adventitial layers of the common carotid artery wall in sonographic images, Comput. Methods Programs Biomed. 67 (2002) 27–37.

[24] M. Kass, A. Witkin, D. Terzopoulos, Snakes: active contour models, Int. J. Comput. Vis. (1988) 321–331.

[25] C.I. Christodoulou, C.S. Pattichis, M. Pantziaris, A. Nicolaides, Texture based classification of atherosclerotic carotid plaques, IEEE Trans. Med. Imaging 22 (7) (2003) 902–912.

[26] D. Barratt, B. Ariff, K. Humphries, S. Thom, A. Hughes, Reconstruction and quantification of the carotid artery bifurcation from 3-D ultrasound images, IEEE Trans. Med. Imaging 23 (5) (2004) 567–583.

[27] M.A. Fischler, R.C. Bolles, Random sample consensus: a paradigm for model fitting with applications to image analysis and automated cartography, Commun. ACM 24 (6) (1981) 381–395.

[28] A.C. Rossi, P.J. Brands, A.P.G. Hoeks, Automatic recognition of the common carotid artery in longitudinal ultrasound B-mode scans, Med. Image Anal. 12 (2008) 653–665.

[29] G.W. Zack, W.E. Rogers, S.A. Latt, Automatic measurement of sister chromatid exchange frequency, J. Histochem. Cytochem. 25 (7) (1977) 741–753.

[30] C. Tauber, Filtrage anisotrope robuste et segmentation par b-spline snake: application aux images échographiques, Ph.D. thesis, Institut National Polytechnique de Toulouse, Toulouse, 2005.

[31] Y. Yu, S. Acton, Speckle reducing anisotropic diffusion, IEEE Trans. Image Process. 11 (11) (2002) 1260–1270.

[32] Y. Yu, S. Acton, Edge detection in ultrasound imagery using the instantaneous coefficient of variation, IEEE Trans. Image Process. 13 (12) (2004) 1640–1655.

[33] M.J. Black, G. Sapiro, D.H. Marimont, D. Heeger, Robust anisotropic diffusion, IEEE Trans. Image Process. 7 (3) (1998) 421–432.

[34] L. Rudin, S. Osher, E. Fatemi, Nonlinear total variation based noise removal algorithms, in: Proceedings of the 11th Annual Int. Conf. of the Center for Nonlinear Studies on Experimental Mathematics: Computational Issues in Nonlinear Science, Elsevier North-Holland, Inc., 1992, pp. 259–268.

[35] L. Rudin, S. Osher, Total variation based image restoration with free local constraints, in: Proceedings of IEEE Int. Conf. on Image Processing (ICIP'94), vol. 1, 1994, pp. 31–35.

[36] J. Canny, A computational approach to edge detection, IEEE Trans. Pattern Anal. Mach. Intell. 8 (6) (1986) 679–698.

[37] Z. Guo, R.W. Hall, Parallel thinning with two-subiteration algorithms, Commun. ACM 32 (3) (1989) 359–373.

[38] R. Burden, J.D. Faires, Numerical Analysis, Brooks Cole, 2000.

[39] D.A. Forsyth, J. Ponce, Computer Vision: A Modern Approach, Prentice Hall, 2003.

[40] A. Marquina, S. Osher, Explicit algorithms for a new time dependent model based on level set motion for nonlinear deblurring and noise removal, SIAM J. Sci. Comput. 22 (2) (2000) 387–405.

[41] O. Chum, J. Matas, J. Kittler, Locally optimized RANSAC, in: Lecture Notes in Computer Science - Pattern Recognition, Springer Berlin/Heidelberg, vol. 2781, Springer LNCS, 2003, pp. 236–243.

[42] J.M. Bland, D.G. Altman, Statistical methods for assessing agreement between two methods of clinical measurement, Lancet 1 (8476) (1986) 307–310.